JACS
JOURNAL OF THE AMERICAN CHEMICAL SOCIETY
pubs.acs.org/JACS
Article

Direct Heat-Induced Patterning of Inorganic Nanomaterials

Haoqi Wu,[‖] Yuanyuan Wang,[‖] Jaehyung Yu, Jia-Ahn Pan, Himchan Cho, Aritrajit Gupta, Igor Coropceanu, Chenkun Zhou, Jiwoong Park, and Dmitri V. Talapin*

Cite This: J. Am. Chem. Soc. 2022, 144, 10495−10506
Read Online

ABSTRACT: Patterning functional inorganic nanomaterials is an important process for advanced manufacturing of quantum dot (QD) electronic and optoelectronic devices. This is typically achieved by inkjet printing, microcontact printing, and photo- and e-beam lithography. Here, we investigate a different patterning approach that utilizes local heating, which can be generated by various sources, such as UV-, visible-, and IR-illumination, or by proximity heat transfer. This direct thermal lithography method, termed here heat-induced patterning of inorganic nanomaterials (HIPIN), uses colloidal nanomaterials with thermally unstable surface ligands. We designed several families of such ligands and investigated their chemical and physical transformations responsible for heat-induced changes of nanocrystal solubility. Compared to traditional photolithography using photochemical surface reactions, HIPIN extends the scope of direct optical lithography toward longer wavelengths of visible (532 nm) and infrared (10.6 μm) radiation, which is necessary for patterning optically thick layers (e.g., 1.2 μm) of light-absorbing nanomaterials. HIPIN enables patterning of features defined by the diffraction-limited beam size. Our approach can be used for direct patterning of metal, semiconductor, and dielectric nanomaterials. Patterned semiconductor QDs retain the majority of their as-synthesized photoluminescence quantum yield. This work demonstrates the generality of thermal patterning of nanomaterials and provides a new path for additive device manufacturing using diverse colloidal nanoscale building blocks.

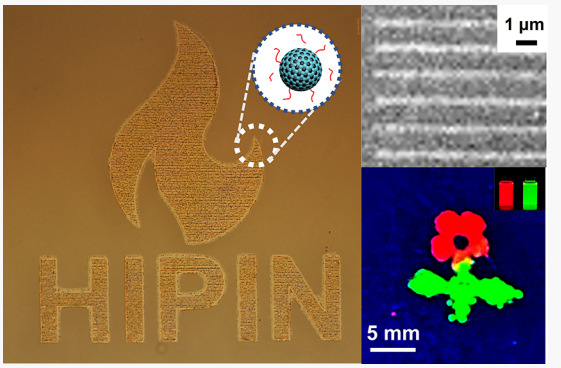

INTRODUCTION

There is a growing number of studies showing that colloidally synthesized quantum dots (QDs) and other functional inorganic nanocrystals (NCs) can offer competitive advantages for a variety of applications, from already broadly commercialized quantum-dot light-emitting diode (QLED) TVs[1] to infrared (IR) cameras in smartphones and self-driving cars,[2] among other electronic and optoelectronic devices.[3−5] Colloidal materials enable device fabrication via solution-based nonepitaxial deposition under ambient environments. To obtain target device structures, material- and process-tailored patterning methods need to be developed with improved resolution, throughput, fidelity, and cost efficiency per patterned element. Various patterning techniques based on inkjet printing,[6,7] optical[8,9] and dip-pen[10] lithography have been developed to optimize these parameters. These approaches typically use colloidal NCs capped with long-chain organic ligands that act as insulating layers blocking efficient charge transport and heat dissipation. Since the performance and stability of nanocrystal-based optoelectronic devices are largely defined by their charge and heat transport properties, new approaches to NC patterning are required.

Direct optical lithography of functional inorganic nanomaterials (DOLFIN) is a methodology for photoresist-free patterning of colloidal NCs using surface ligands designed to chemically transform upon exposure to light (typically UV) or an electron beam.[11−13] NC solubility is altered by this surface modification, forming distinct patterns between the exposed and unexposed regions. The ligands for DOLFIN can be engineered to be sensitive to different UV and blue spectral regions (254−450 nm) and suitable for various nanomaterials and solvents. Like any other patterning method, DOLFIN has limitations. One is imposed by limited penetration of UV light into nanomaterials that strongly absorb in that spectral region. This reduces the thickness of patternable metal and QD films, and it can be partially addressed by implementing high-exposure dose or multistep patterning but often at the expense of throughput and pattern quality.[14,15] The lateral resolution of DOLFIN patterns is further limited by the Abbe diffraction limit and by blurring of pattern edges due to light scattering during exposure. Despise intense research into novel photosensitizers and photoacid generators for general photolithographic applications, their quantum efficiency is typically 10−

Received: April 7, 2022
Published: June 9, 2022

https://doi.org/10.1021/jacs.2c03672
J. Am. Chem. Soc. 2022, 144, 10495−10506

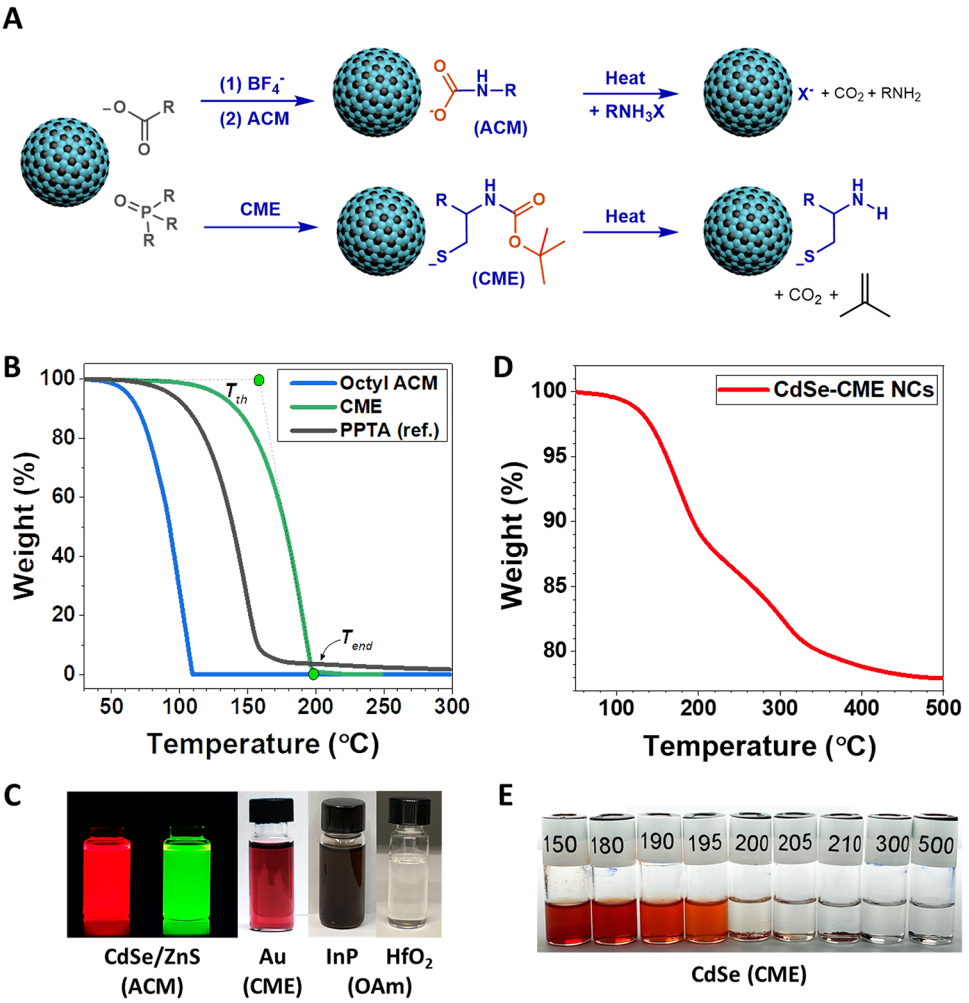

Figure 1. Chemical structure and thermal decomposition of thermally sensitive ligands on nanocrystal surface. (A) Chemical structures of thermally sensitive ligands and schematics of their use in NC patterning: ammonium carbamate (ACM) and *N*-(*tert*-butoxycarbonyl)-L-cysteine methyl ester (CME) applied to exchange the original ligands at nanocrystal surface and corresponding thermally triggered surface reactions. (B) Thermogravimetric analysis (TGA) curves for octyl-ACM and CME ligands compared to the standard thermal resist material polyphthalaldehyde (PPTA). The temperature ramp rate is 5 °C/min. The decomposition threshold temperature (T_{th}) and the end point temperature (T_{end}) are indicated as green dots. (C) Colloidal solutions of different nanocrystals capped with various thermally sensitive surface ligands. (D) TGA curve of CdSe-CME nanocrystals at the ramp rate of 5 °C/min and (E) nanocrystal solubility test in the developer solvent $CHCl_3$/EtOH (v/v = 4:1) after heating to various temperatures at the same ramp rate (5 °C/min). The final temperatures from left to right were 150, 180, 190, 195, 200, 205, 210, 300, and 500 °C.

20% and most of light energy is lost as heat.[16] Utilization of this heat may create new opportunities for nanomaterial patterning.

Recently, thermal lithography has attracted attention as a possible alternative to photolithography. Thermal scanning probes and pulsed lasers are used to induce localized temperature jumps, patterning materials through thermal ablation, crystallization, phase change, etching, oxidation, decomposition, or structural conversion of the target.[17−21] Thermal lithography is potentially capable of breaking the Abbe diffraction limit for patterning nanoscale features. For example, upon pulsed illumination with a laser beam focused into a diffraction-limited spot, fast nanoscale heat transfer creates a large transient temperature jump in the center of the illuminated spot relative to the temperature of the surrounding area. Only a small subset of the illuminated region reaches the threshold temperature, so sub-beam size resolution can be achieved.[22] Our previous study shows that the low thermal conductivity of NC and QD layers[23] suppresses lateral heat diffusion and hence is favorable for pattern resolution.

A wide range of materials can be thermally patterned, including polymer resists,[24] metal−organic frameworks,[17] phase change materials,[20] two-dimensional (2D) materials,[25] and biomolecules.[26] Thermal patterning has also been applied to nanoparticles. Most of the work on thermal patterning of nanomaterials has used thermal scanning probes, e.g., Lee et al. used a hot tip to pattern polymer−nanoparticle composites.[27] In an early work by the Prasad group, silver nanoparticles with thermally sensitive *N*-(*tert*-butoxycarbonyl)-L-cysteine methyl ester (CME) ligands were patterned using two-photon femtosecond illumination.[28] Huang et al. prepared patterns of plasmonic silver nanoparticles through local decomposition of silver nitrate salt.[29] Ooms et al.[30] patterned gold nanoparticles through heat-induced sintering. Consideration of these references shows an obvious lack of work on thermal patterning of functional nanomaterials using high-throughput and scalable optical techniques.

https://doi.org/10.1021/jacs.2c03672
J. Am. Chem. Soc. 2022, 144, 10495−10506

Inspired by the success of DOLFIN chemistry,[11,12] we focused on designing new thermally sensitive ligands that can be applied to a broad scope of functional inorganic nanomaterials. Here, we introduce the direct heat-induced patterning of inorganic nanomaterials (HIPIN) method, which can directly pattern NCs of various metals, dielectrics, and semiconductors using 10.6 μm CO_2 laser light, proximity heat from LED pixels, 405 nm continuous wave (CW) and 532 nm pulsed lasers, and heated stencils. Volatile amine ligands, thermally sensitive and engineerable ammonium carbamates (ACMs), or *N*-(*tert*-butoxycarbonyl)-L-cysteine methyl ester (CME) ligands are used to thermally pattern NCs and QDs while preserving their size and morphology. HIPIN also can achieve diffraction-limited features (~480 nm) at a numerical aperture (NA) of 0.7 using a 532 nm (green) laser. Finally, we observe that the decrease in the photoluminescence quantum yield (PLQY) of core−shell QDs is small following the HIPIN process, which is promising for fabricating high-performance QD LEDs and other optoelectronic devices.

RESULTS AND DISCUSSION

Designing Thermally Sensitive Ligands for HIPIN. We explored three families of thermally sensitive surface ligands: ammonium carbamates (ACMs), alkylamines, and methyl esters—specifically, *N*-(*tert*-butoxycarbonyl)-L-cysteine methyl ester (CME). These ligands have different thermal properties and different decomposition thresholds. They also have distinct binding affinities, making them compatible with different types of inorganic NCs.

ACM compounds have been actively researched for CO_2 sequestration technologies due to their structure-dependent thermal decomposition properties.[31] These ligands can be easily prepared by adding CO_2 in form of dry ice to primary or secondary amines. Aliphatic ACM compounds are transparent throughout most of the UV−vis region and hence are not suitable for use as photosensitive ligands (Figure S1). However, they can be used as thermally sensitive ligands due to their facile decomposition back into CO_2 and the corresponding amine (Figure 1A, top). Generally, an increase in the bulkiness of the alkyl group leads to a higher decomposition threshold, which allows for a thermally engineerable decomposition threshold in the range of 50 °C to above 100 °C (Figures 1B (blue), S2, and Table 1).

CME was first studied by the Prasad group as a thermally cleavable ligand for metal NCs.[28] This ligand has a labile *tert*-butoxycarbonyl group that thermally decomposes into CO_2 and isobutene upon sufficient heating, leaving behind secondary amine (Figure 1A, bottom). Compared to ACM ligands, CME has a higher decomposition threshold of about 160 °C (Figure 1B, green). This means that more heat needs to be applied to induce ligand decomposition, leading to less thermally sensitive nanocrystal inks. This insensitivity can be advantageous for room temperature stability.

Table 1. T_{th} and T_{end} Summary of Various ACM, CME, and Polyphthalaldehyde (PPTA) Ligands (Ramp: 5 °C/min)

ACM type	T_{th} (°C)	T_{end} (°C)	range (°C)
methyl-ACM	52	76	24
butyl-ACM	50	71	21
isopentyl-ACM	52	69	17
pentyl-ACM	64	93	29
hexyl-ACM	68	91	23
octyl-ACM	77	104	27
dibutyl-ACM	58	78	20
cyclohexymethyl-ACM	85	93	8
propylene diamino-ACM	102	126	24
CME	161	197	24
ref PPTA	119	158	39

The thermal decomposition behavior of ACM and CME ligands used in this study can be compared with that of thermal resist polyphthalaldehyde (PPTA) commonly used in thermal scanning probe lithography.[32,33] PPTA has a decomposition threshold of about 120 °C (Figure 1B, gray), making it more thermally sensitive than CME but less thermally sensitive compared to ACMs. Importantly, we also compared the thermal decomposition temperature window (defined as the difference between T_{end} and T_{th} in Figure 1B) of these compounds and found that both ACMs and CME have a narrower temperature window between the start and completion of thermal decomposition (between 8 and 29 °C) compared to PPTA (39 °C). This implies that the thermal decomposition contrast of ACMs and CME is comparable to or even better than that of PPTA. In addition, PPTA also leaves more residue (~5 wt %) after approaching its decomposition end point, T_{end}, compared to both ACMs (typically <0.5 wt %) and CME (~1 wt %). This observation suggests that ACM and CME molecules are not prone to side reactions besides their main decomposition pathways outlined in Figure 1A.

To prepare thermally patternable NC inks, the heat-sensitive ligands need to be attached to the NC surface. The details of surface exchange depend on the specific interactions between the ligand and the NC surface. For ACM ligands, the binding affinity of the carbamate group to the NC surface is not sufficiently strong to displace native carboxylate or phosphonate ligands. Hence, we adopted a two-step process that first involved the removal of native ligands using a stripping agent like nitrosonium tetrafluoroborate ($NOBF_4$)[34] or triethyloxonium tetrafluoroborate (Meerwein's salt, Et_3OBF_4)[35] to prepare "bare" NCs (Figure 1A, top). We then introduced ACM ligands to the bare NCs to prepare colloidal NCs capped with ACM (Figure 1C and Scheme S1). This ink maintains high colloidal stability in chloroform, chlorobenzene, and dichlorobenzene, e.g., up to concentrations of about 130 mg/mL in chlorobenzene. As a demonstration of the thermal instability of this ink, a solution of CdSe NCs in $CHCl_3$/EtOH (v/v = 4:1) capped with ACM ligands turns cloudy upon heating to 100 °C (Figure S3). Interestingly, the NCs become colloidal again upon the addition of more ACM, showing that the NC surface remains accessible after ligand decomposition.

For CME, the stronger binding affinity of its thiol group to the NC surface allows for a more straightforward one-step ligand exchange that produces stable colloidal NC solutions (Figure 1A (bottom),1C).[28] This one-step process avoids using acidic and oxidative stripping agents, which may create surface defects that decrease the luminescence efficiency of semiconductor QDs. This is important for the fabrication of patterned light-emitting diodes and color filters for display applications.

CdSe NCs capped with CME (Figure S4) showed clear weight loss in TGA measurements associated with the decomposition of CME ligand (Figure 1D). However, compared to the decomposition of pure CME ligand, the decomposition of CME bound to the NC surface showed two

https://doi.org/10.1021/jacs.2c03672
J. Am. Chem. Soc. 2022, 144, 10495−10506

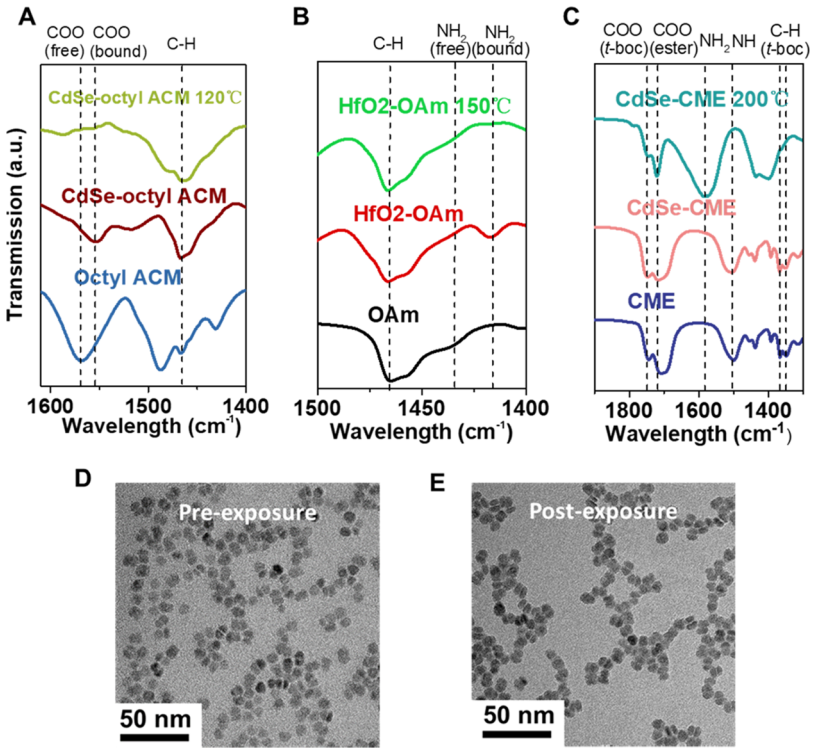

Figure 2. Properties of nanoparticles with HIPIN ligands. Fourier transform infrared (FTIR) spectroscopy spectra of (A) octyl-ACM and CdSe-octyl-ACM before and after heating at 120 °C for 5 min. All samples are drop-cast onto ZnSe substrates for FTIR measurement. (B) Oleylamine and as-synthesized HfO_2 NCs with oleylamine ligands before and after heating at 150 °C for 3 min. (C) *N*-(*tert*-Butoxycarbonyl)-L-cysteine methyl ester (CME) and CdSe NCs with CME ligands before and after heating at 200 °C for 3 min. Transmission electron microscopy (TEM) images of CdSe/ZnS core−shell quantum dots (QDs) with CME ligands before (D) and after (E) exposure to 400 mW, 10 ns-pulsed laser.

distinct steps, each corresponding to a weight loss of about 11%. This is consistent with the decomposition of CME (MW = 235.30) into 3-mercaptopropanoate (MW = 120.17) during the first step, with the second decomposition step probably being attributable to the further decomposition of 3-mercaptopropanoate and thiolation of the NC surface.[36] The second dissociation step occurs at a significantly higher temperature than the boiling point of 3-mercaptopropanoate (bp 166 °C) due to the strong interaction of the ligand with the metal cations on the NC surface. TGA analysis also allows us to estimate the surface ligand density of CME to be about 3.5 ligands/nm^2.

We first studied how the thermal decomposition of NC surface ligands affects their colloidal stability. CdSe-CME NCs were heated to various temperature points in the TGA instrument (with a ramp rate of 5 °C/min) and then rapidly cooled (e.g., the temperature dropped from 200 to 120 °C within 1 min). For each temperature end point, we attempted to disperse the preheated NC solids in $CHCl_3$/EtOH (v/v = 4:1) mixture, which we used as a developer solvent for HIPIN (Figure 1E). It can be clearly seen that there is a sharp solubility change between NCs heated to 195 °C with those heated to 200 °C. From the TGA curve, this 5 °C window corresponds to only a 0.57 wt % drop (from 89.85 to 89.28 wt %), which can be attributed to the decomposition of a mere 5% (0.57/11.12) of CME into 3-mercaptopropanoate. This implies that a very small change in the ligand decomposition fraction can have a dramatic effect on NC solubility, and such nonlinearity is desirable for thermal patterning with high resolution and sharp edge contrast. We also noticed that after heating to 200 °C for 3−5 min, CdSe-CME NCs can colloidally disperse in another solvent mixture ($CHCl_3$/EtOH, v/v = 1:4) that was not originally a good solvent for the CME-CdSe NCs (Figure S5), possibly due to the polarity change of the ligands. This observation implies that thermally sensitive NC inks can be suitable for dual-tone patterning. This is an important quality because the remaining nanomaterial is not exposed to high temperature, e.g., photoluminescence (PL) undergoes additional quenching because of surface trapping by the thermally created surface defects.[37]

NCs capped natively with *n*-alkylamine ligands, e.g., InP and HfO_2 NCs capped with oleylamine (Figure 1C), can also be thermally patterned (without any additional ligand exchange) because amines are weakly bound L-type ligands and can partially dissociate from the NC surface upon heating. In contrast, NCs that are capped with more strongly bound L-type or X-type ligands (e.g., trialkylphosphine oxide or oleate) cannot be thermally patterned without destroying the NC cores. Strongly bound X-type native ligands can be exchanged with amines to enable thermal patternability, but we found it difficult to obtain good colloidal stability at high NC concentrations while using labile amine ligands.[38]

Probing Heat-Induced Transformations of Nanocrystal Surface. After heating the CdSe-ACM film to 120 °C on a hot plate, we observed a diminishing of the peak intensity for bound carboxylate (−COO−) groups on the surface of CdSe-ACM NCs, as measured using Fourier transform infrared (FTIR) spectroscopy. The suppression of a band at 1558 cm^{-1} (Figure 2A) indicates complete decomposition of ACM into free amine ligands, which are weakly bound L-type ligands and are not able to remain on the NC surface after heat treatment. This dissociation results in

https://doi.org/10.1021/jacs.2c03672
J. Am. Chem. Soc. 2022, 144, 10495−10506

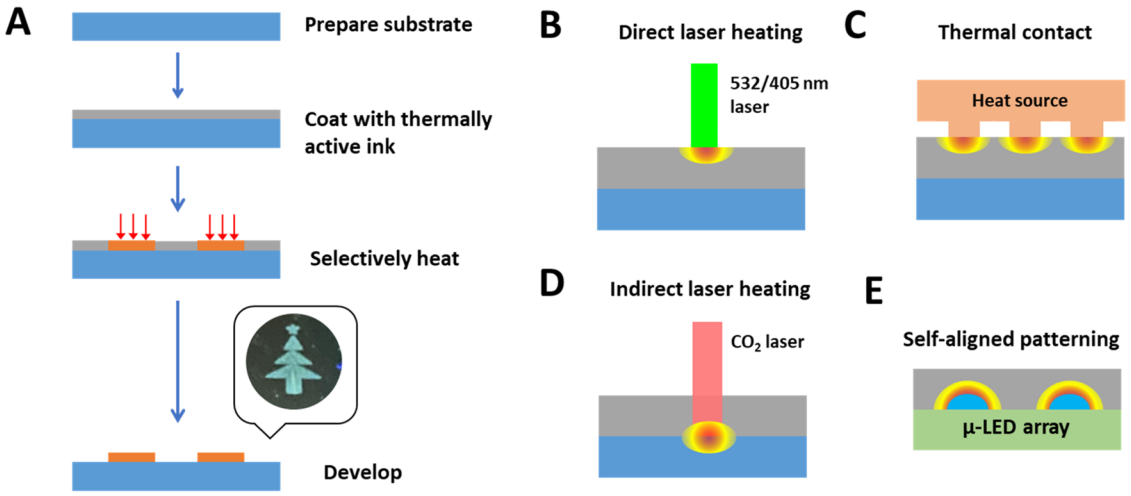

Figure 3. Heat-induced patterning of inorganic nanocrystals (HIPIN). (A) General scheme of HIPIN process. (B–E) Various heating sources for HIPIN: (B) pulsed or continuous-wave laser light can be absorbed by the material in the patterned layer; (C) thermal contact can transfer heat to material in the patterned layer; (D) patterned layer can be transparent to the laser beam (e.g., 10.6 μm IR CO_2 laser), but the heat generated in the substrate underlying can be transferred to the patterned nanocrystal layer by conduction; (E) a heat source (e.g., heat generated by a light-emitting diode, heated cantilever, or hot stencil) can be transferred to the patterned material layer to induce local thermal transformation of surface ligands.

Table 2. Tested NC-Ligand Combinations and Patterning Conditions

ligand	material	solvent	developer	temperature (°C)
oleyamine	CdSe, HfO_2, InP/ZnS, Au	toluene, chlorobenzene	chloroform	150–200
ACM	CdSe, CdSe/ZnS	chlorobenzene	chloroform, chlorobenzene	80–150
CME	CdSe, CdSe/ZnS, HfO_2, Au	chloroform, chlorobenzene	chloroform/ethanol	150–200

changes of the NC solubility in a nonpolar solvent. Similarly, L-type oleylamine is a weakly bound ligand and can readily dissociate from the NC surface upon heating, and the degree of dissociation strongly depends on the heating temperature. FTIR spectra showed that the bound amine ($-NH_2$) peak at 1419 cm^{-1} of HfO_2-oleylamine NCs nearly disappeared after heating to 150 °C (Figure 2B).[38] Upon heating NCs protected with CME ligands, the ratio of the peak associated with *tert*-butyloxycarbonyl (*t*-boc) carboxylate groups to that of the ester group decreased, as did the ratio of the intensities of imido ($-NH$) to amino ($-NH_2$) vibrational signals. The reduction of the relative intensities corresponding to bound surface groups, as well as the disappearance of bands from the C–H bonds in the *t*-boc group, supported the thermal ligand decomposition pathway proposed in Figure 1A (Figure 2C).

The ligand transformations can be carried out without introducing significant changes in NC morphology. Transmission electron microscopy (TEM) images show no NC sintering or necking after the laser exposure, though the distance between neighboring NCs became smaller due to the transformation or evaporation of thermally sensitive ligands (Figure 2D,E).

Heat-Induced Patterning of Inorganic Nanocrystals. To obtain two-dimensional HIPIN patterns, the NCs need to be deposited as a film and then subjected to local heating (Figure 3A). This heat treatment changes the colloidal solubility of NCs, allowing patterns to emerge upon development with a suitable solvent (e.g., a Christmas tree in Figure 3A, inset). The combinations of NCs and thermally sensitive surface ligands are shown in Table 2, along with their patterning conditions, such as the solvent for NC ink, developer, and temperature.

In this study, we explored several approaches to supply heat to the NC film: direct laser heating, indirect laser heating, and proximity heat transfer. Each of these approaches has different degrees of spatial and temporal control of the heating profile, leading to variations in the pattern resolution. Obviously, better control over the heating profile is desirable, but this can involve cost and throughput tradeoffs.

Direct laser heating involves scanning continuous wave (CW) or pulsed laser beams across a highly absorbing NC film (Figure 3B). To get high-resolution patterns, we utilized a 10 ns-pulsed 532 nm laser scanning system coupled with a homebuilt microscope. With this system, we successfully patterned CdSe-CME NCs with good contrast and feature sizes down to below 500 nm, as characterized by scanning electron microscope (SEM, Figures 4A,C and 5C) imaging. We also patterned luminescent InP/ZnSe/ZnS-OAm NCs, showing the generality of this process (Figure 4B). Typically, 532 nm light cannot be used for direct patterning NCs that do not absorb at this wavelength (e.g., green-emitting CdSe/CdZnS QDs), but this limitation can be overcome using a laser with a shorter wavelength. For example, a 405 nm CW laser can generate high-contrast patterns on different materials (Figure 4D).

Another way to supply heat to the NC film is through an indirect laser heating process (Figure 3D). In this approach, a CO_2 laser can be used to heat the underlying substrate which subsequently transfers heat to the NC layer. CO_2 lasers are widely used in industry to produce mid-infrared (IR) light with principal bands centering at 9.4 and 10.6 μm. They can have a high power density, 5–100 W mm^{-2}, and can be rapidly scanned. An advantage of this indirect approach is that any NCs with thermally sensitive ligands can be patterned on a

https://doi.org/10.1021/jacs.2c03672
J. Am. Chem. Soc. 2022, 144, 10495–10506

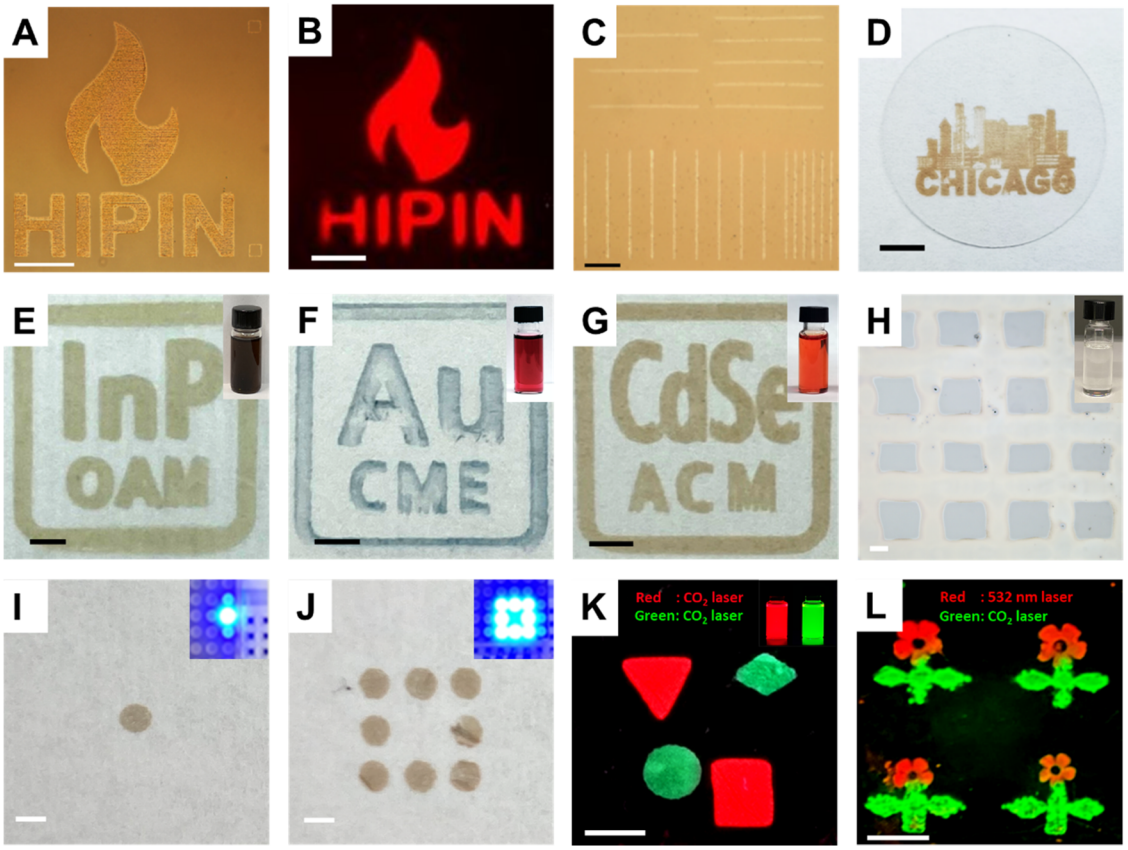

Figure 4. Examples of thermally patterned inorganic nanomaterials. (A) CdSe QDs patterned using CME ligands (10 ns, 20 mJ cm^{-2}), (B) InP/ZnS core−shell QDs with oleylamine ligands (10 ns, 150 mJ cm^{-2}), and (C) line patterns of CdSe QDs with CME ligands patterned (10 ns, 25 mJ cm^{-2}) using a 532 nm pulsed laser. (D) CHICAGO pattern made from CdSe QDs using a 405 nm CW laser. (E−H) Different colloidal NC inks patterned using a CW CO_2 laser (10.6 μm): (E) InP-oleylamine, (F) Au-CME, (G) CdSe-ACM, and (H) HfO_2-oleylamine NCs. The inset images show photographs of the corresponding thermally sensitive inks. (I, J) Self-aligned patterning of CdSe-CME NCs using local heat generated by an array of blue (460 nm) light-emitting diodes turned on in two different patterns. (K) CdSe/ZnS QDs with ACM ligands used for a dual-color pattern. (L) InP/ZnSe/ZnS QDs with oleylamine ligands (red) and CdSe/ZnS QDs with ACM ligands (green) patterned using 532 nm pulsed and CO_2 CW lasers, respectively. Scale bars in panels (A)−(C) and (E)−(H) are 100 μm; in panels (D), (I)−(L), 1 cm.

suitable substrate regardless of the light absorption properties of the NCs themselves.

Suitable substrates for CO_2 laser patterning can be chosen based on the following requirements: (1) strong absorption at 10.6 μm to convert photon energy to heat; (2) low thermal conductivity to limit heat dissipation and increase local temperature; and (3) resistance to nonpolar solvents. Based on these criteria, borosilicate glass is a good substrate for HIPIN, as it can fully absorb 10.6 μm light (Figure S6), has a relatively low thermal conductivity (1.05 W/(m K)), is stable toward all common solvents, and is already widely used in micro- and nanofabrication (Table S1). We were able to pattern InP-OAm NCs, Au-CME NCs, CdSe-ACM NCs, and HfO_2-OAm NCs on glass using a commercial CO_2 laser scanner (Figure 4E−H). We obtained feature sizes below 200 μm, with the resolution being limited by the beam size of our CO_2 laser, estimated to be about 375 μm (see Section S3 in the Supporting Information, along with Figures S13−S15, for details on the characteristics and testing of the commercial CO_2 laser).

Thermal patterning of NCs can also be realized by a direct heat transfer from a proximal hot object (Figure 3C), such as a heated cantilever[18] or stencil. For example, we pressed an aluminum stencil preheated to 350 °C against a film of HfO_2-OAm NCs for 5 s, resulting in a pattern formed upon development with chlorobenzene (Figure S7). This control experiment nicely demonstrates that the solubility change of our NC films is achieved with heat alone, irrespective of light exposure.

NC patterning by proximity heating offers an interesting opportunity for self-aligned patterning of quantum dots using local heat generated by blue InGaN LEDs (Figure 4I,J). An increase of the local temperature near a blue LED upon turning it on can be recorded using a thermal camera (Figure S8). This heat is sufficient to pattern a film of CdSe-isopentyl-ACM NCs with about 60 s exposure time at the contact temperature of ∼60 °C provided by our low-power blue LEDs. By switching different pixels on and off, we generated different patterns of CdSe quantum dots (Figure 4I,J). This approach could be particularly interesting for patterning quantum dot color conversion filters for μ-LED arrays.[39] Such μ-LED displays are currently under development for various display applications, and local heating of μ-LED surface to more than 100 °C is routinely observed,[39] which can be utilized for self-aligned patterning of color-converting quantum dot layers with micron resolution (Figure 3E).

It is noteworthy that different NCs can be patterned on the same substrate by sequential patterning steps. Multicolor patterning is important for optoelectronic applications, such as QLED displays. For example, red- and green-emitting CdSe/

https://doi.org/10.1021/jacs.2c03672
J. Am. Chem. Soc. 2022, 144, 10495−10506

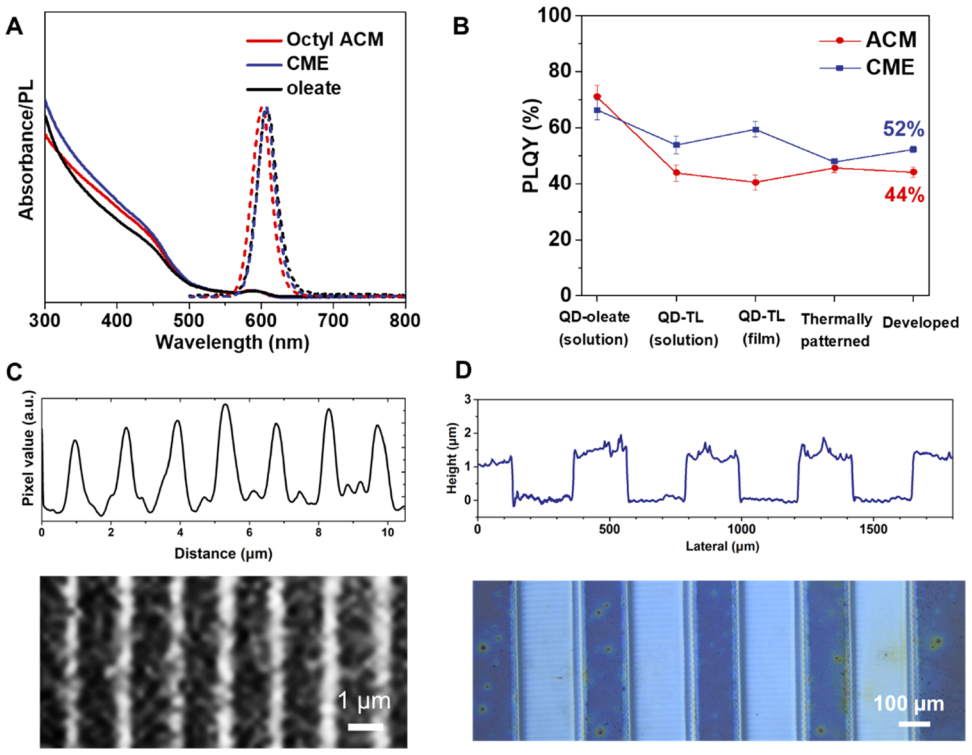

Figure 5. Properties of thermally patterned QDs. (A) Ultraviolet−visible absorption and photoluminescence (PL) spectra of CdSe/ZnS quantum dots with native oleate and thermally sensitive ligands. (B) Evolution of PL quantum yield for CdSe/CdS/ZnS QDs at different stages of the HIPIN process: pristine QDs with oleate ligands, QDs exchanged with thermally sensitive octyl-ACM and CME ligands in solution and film, and QDs exposed by CO_2 laser (1 W at 200 mm/s scanning speed) and after treatment with developer solvent. (C) SEM image (bottom) and its corresponding line profiles (top) extracted from the image of CdSe-CME stripe pattern with 480 nm linewidth (developer CH_3Cl/EtOH = 4:1). (D) 200 μm pitch and 1.2 μm thickness CdSe stripes patterned by green pulsed laser and corresponding height profile (developer CH_3Cl/EtOH = 1:4).

ZnS-octyl ACM NCs were patterned in two steps using CO_2 laser heating (Figure 4K). Furthermore, different patterning tools can be used for each step, as shown by the patterning of green-emitting CdSe/ZnS-ACM NCs by indirect CO_2 laser heating, followed by the patterning of red-emitting InP/ZnSe/ZnS-OAm NCs by direct 532 nm laser heating (Figure 4L). The heat-induced surface modification makes it possible for the first-deposited green-emitting QDs to retain the pattern without getting dissolved upon the subsequent patterning process of red-emitting QDs.

The exchange of native oleate ligands for thermally sensitive ACM and CME ligands did not dramatically change the absorption of core−shell QDs in the ultraviolet and visible spectrum, as shown by our investigation of the photoluminescence quantum yield (PLQY) after each step of the HIPIN process (Figure 5A,B). For one particular set of conditions, we found that after ACM ligand capping, the absorption spectrum is well maintained, and PL slightly blue-shifts, while the solution PLQY dropped from 70.9 ± 4.2% (oleate) to 43.8 ± 2.9% (octyl ACM), which may be due to partial surface etching during the ligand stripping. The film fabrication slightly decreased PL, possibly due to Foerster energy transfer between NCs introducing additional PL quenching. After the laser treatment, the film PL increased, which was attributed to defect annealing. PLQY decreased after the final step development, since the weakly bound amine ligands could be partially washed off by the developer. CME ligands generally enabled higher PLQYs, which we attribute to a stronger binding ability of CME ligands to the NC surface. This stronger binding allowed us to directly exchange the original oleate ligands with CME, avoiding the intermediate step of ligand stripping. We did not observe any shifts of the PL peak when using CME ligands, and the solution PLQY dropped from 66.3 ± 3.6% (oleate) to 53.8 ± 3.2% (CME). The photoluminescence measurements showed significantly improved PLQY after patterning with HIPIN relative to that from our previous optical patterning methods (Table S2).[11−13]

High-Resolution Patterning of Nanocrystals by HIPIN. To explore the feasibility of high-resolution HIPIN patterning, narrow lines of CdSe NCs were thermally patterned using a homebuilt optical setup equipped with an objective with a numerical aperture (NA) of 0.7. The theoretical diffraction-limited resolution of an imaging system can be defined by the point spread function. The radius of the airy disk $d \approx 0.61\lambda/NA$ = 464 nm is close to the full width at half maximum (fwhm) of the point spread function, and this number can be used as the diffraction-limited linewidth. When CdSe NC stripes were patterned on a glass substrate, the linewidth patterned by HIPIN was ∼570 nm (Figure S11A). According to the simulation results presented in the following sections, substrates with higher thermal conductivity facilitate prompt cooling of the patterned layer and therefore should be favorable for achieving a higher pattern resolution. Thus, we chose to pattern CdSe stripes using an indium tin oxide (ITO)-coated glass substrate, the thermal conductivity of which is ∼4 times higher than the thermal conductivity of borosilicate glass. With the same patterning settings, we achieved ∼480 nm linewidth measured as fwhm of the peaks in

https://doi.org/10.1021/jacs.2c03672
J. Am. Chem. Soc. 2022, 144, 10495−10506

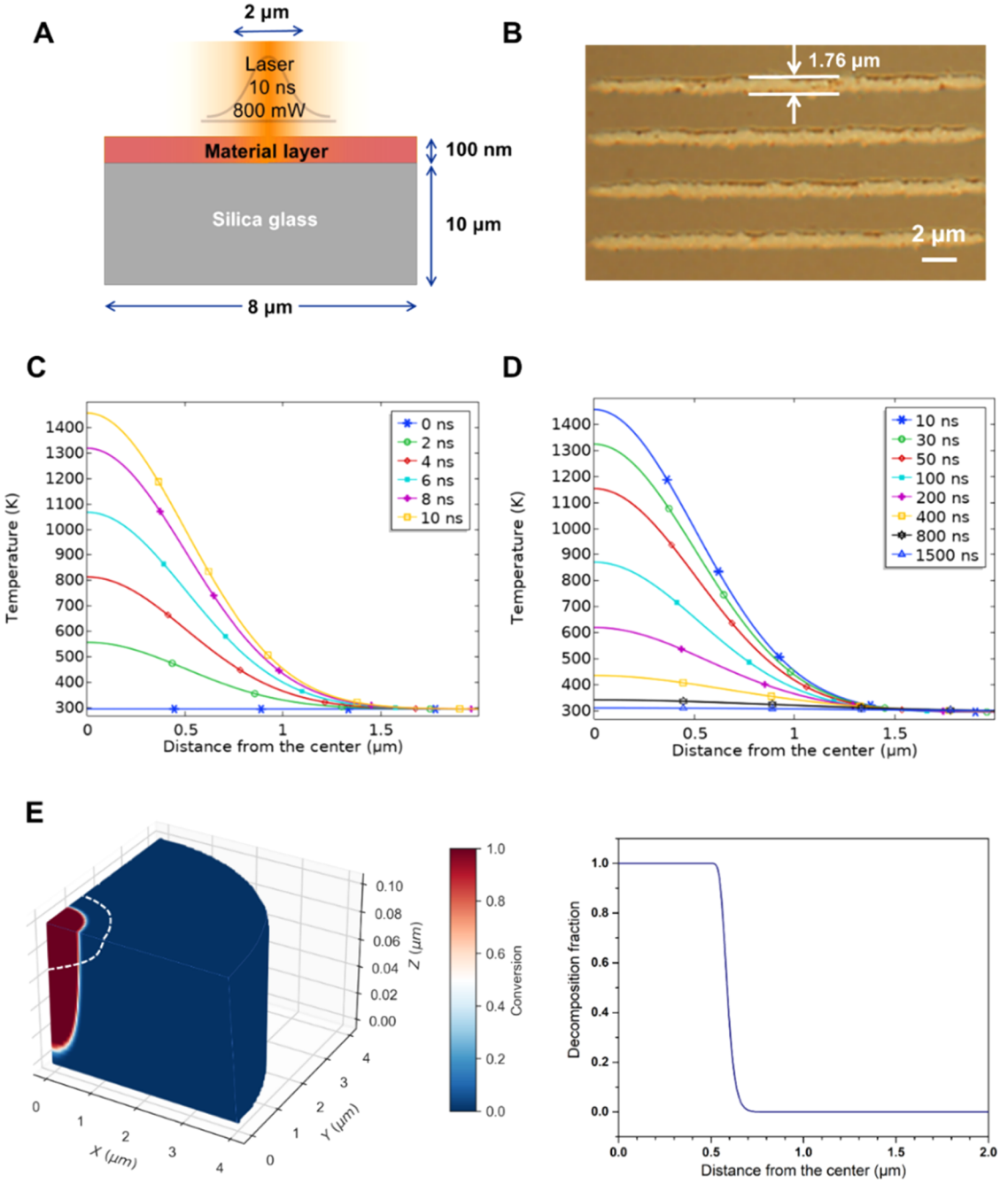

Figure 6. Modeling HIPIN temperature profile and patterning resolution. (A) Scheme of the volumetric heat source model (VHS): 100 nm thick CdSe nanocrystal film (absorption coefficient 2.5×10^4 cm^{-1}, emissivity 0.6, reflectance 0.8) coated on a silica glass and exposed with green 532 nm Gaussian beam ($\sigma = 1$ μm) for 10 ns with 800 mW peak power. (B) Experimental pattern of CdSe NCs using 2 μm diameter green pulsed laser light. (C, D) Simulations of the in-plane temperature distribution on top of CdSe NC film during (C) laser heating period and (D) film cooling period. (E) Ligand conversion fraction (C) calculated at each point throughout CdSe NC film (left) and C versus distance from the beam center (right). The white dashed line is the $1/e^2$ light iso-intensity profile corresponding to $\sigma = 1$ μm from the center.

SEM image line scan (Figures 5C and S11B). This linewidth matched, within experimental uncertainty, the theoretical fwhm of diffraction-limited point spread function of our imaging system. Based on our modeling described in the following sections and previous experimental studies of other types of thermal resists,[22] HIPIN should be capable of exceeding the optical diffraction limit after optimizing thermal diffusion parameters and film thickness and applying NC ligands with larger activation energies for the thermal decomposition reaction. Switching to ultrashort laser pulses and using multiple pulses to expose the same area offer additional opportunities for achieving thermal patterning with sub-diffraction resolution.[20]

Thick-Layer Patterning of Nanocrystals by HIPIN. Some applications require patterning thick NC films. For example, for display applications, QD color conversion filters need to efficiently absorb the blue light from μ-LED or liquid-crystal display (LCD) backlighting panels, with an optical density of 2 or more at the excitation wavelength. The DOLFIN method relies on the photochemical reactions of surface ligands, and

https://doi.org/10.1021/jacs.2c03672
J. Am. Chem. Soc. 2022, 144, 10495−10506

the light used for optical patterning must penetrate through the full thickness of the NC layer. For materials like QDs with high absorption in UV, light penetration becomes the limiting factor that defines the photochemical patternability of thick QD layers (Figure S9). In contrast, HIPIN provides significant flexibility for patterning thick layers of light-absorbing NCs because (i) the exposure wavelength is not defined by the ligand absorption spectrum but can be tailored to provide a desired tradeoff between the absorption (and heating) efficiency and light penetration depth and (ii) the heat flow inside the NC film does not cease immediately when illumination is off. Instead, photogenerated heat can diffuse throughout the NC film into the substrate. As a proof of concept, we blade-coated CdSe QDs with CME ligands onto a glass substrate to make a thick film, and we used 532 nm pulsed laser to write stripe patterns followed by development in CH_3Cl/EtOH solution (v/v = 1:4). This resulted in a QD film with a thickness of over 1 μm (Figure 5D). HIPIN can be used to pattern micron-thick films of light-absorbing materials, such as metals, oxides, core−shell QDs, etc., for light conversion and other applications (Figure S12), which are not easy to pattern at such thicknesses with single-step DOLFIN[11] or traditional photolithography.

Modeling Heat Flow and Surface Reaction Kinetics. In HIPIN, the solubility contrast develops through the convolution of time- and temperature-dependent reaction kinetics, making thermal lithography different from DOLFIN and traditional photolithography utilizing light-sensitive polymers. For example, when the temperature is close to the onset temperature for ligand transformation, it takes several minutes to generate HIPIN patterns. However, an intense pulsed laser can promptly generate a hot spot with a very high local temperature, but heating and cooling around this spot can occur on the time scale of nanoseconds to microseconds. As we show below, this transient heating and cooling can enable high-resolution patterning. This effect depends on the ligand decomposition kinetics, which should be modeled quantitatively to describe the temperature and reaction kinetic profiles inside patterned NC layers.

Kinetics of Ligand Thermal Decomposition. HIPIN patterning can use conversion or desorption of NC surface ligands. These processes can also happen together, either successively or simultaneously. In Figure 1D, we demonstrated that the thermal decomposition of CME ligands is responsible for the solubility change of CdSe NCs, and this material system is chosen here as an example. To first order, the analysis can be simplified into investigating thermal decomposition kinetics of pure CME ligands. To estimate thermal decomposition kinetics, we carried out thermogravimetric studies of CME decomposition at different heating rates (Figure S10A). The decomposition rates can be related by the Arrhenius equation[40]

$$\frac{dC}{dT} = \frac{Z}{\beta} f(C)\, e^{-(E_a/RT)} \tag{1}$$

where C is the fraction of thermally converted CME ligand, T is temperature, Z is a pre-exponential factor, β is the heating rate (temperature ramp), $f(C)$ is a function of the conversion fraction, depending on the reaction order (typically first order for thermal decomposition), R is the ideal gas constant, and E_a is the activation energy. At a constant C and $E_a/RT > 20$, the eq 1 can be expressed as[40]

$$\frac{d\ln\beta}{d\left(\frac{1}{T}\right)} = \frac{R}{0.457} E_a \tag{2}$$

The linear relationship between $\ln\beta$ and $1/T$ provides a reasonable fit (Figure S10B) with an activation energy E_a = 168 kJ mol^{-1} and pre-exponential factor $Z = 1.6 \times 10^{17}$ s^{-1}, assuming first-order reaction kinetics.[41] With the above kinetic information, the time to complete conversion ($C > 95\%$) can be calculated for different temperatures (Table S3). This information is useful for determining the threshold for an isothermal patterning process. For example, it takes 10 min to decompose CME ligands at 400 K but only 11 ns at 1000 K. However, isothermal kinetics cannot fully describe the HIPIN process with complex time-dependent temperature profiles. Hence, we modeled the full temperature profile and convoluted it with the surface reaction kinetics.

Modeling Temperature Profiles in Nanocrystal Layers. To understand the heat flow and time-dependent temperature distribution in NC layers exposed to a laser beam, we used the volumetric heat source (VHS) model as implemented in the COMSOL Multiphysics package to simulate HIPIN patterning of CdSe QDs with a nanosecond pulsed 532 nm laser. The model is schematically presented in Figures 6A and S16. The optical energy of the laser beam can be absorbed by the material being patterned, transmitted into the substrate, or reflected. For the normal incidence of 532 nm laser light, the reflectivity (R) or CdSe NC layer can be calculated as $R = \frac{(1-n)^2}{(1+n)^2}$, where n and k are the real and imaginary components of the complex refractive index. We used the literature values in our model.[42] The light absorption follows the Beer−Lambert law $\frac{dI}{dh} = -\alpha I$, where I is the laser light intensity, h is the depth from the film surface, and α is the linear absorption coefficient, implying that light intensity decays exponentially inside the patterned layer (Figure S9). The value of $\alpha \sim 2.5 \times 10^4$ cm^{-1} at 532 nm corresponds to a typical value for absorption in CdSe NC film.[43]

Only a fraction of absorbed light energy is converted into heat. The absorbed light can generate photoluminescence, and, for well-optimized synthetic protocols, core−shell QDs can achieve near-unity PLQY.[44] However, even for a perfect QD emitter, localized heating will be produced from the Stokes shift (difference between the energy of absorbed and emitted photons). Moreover, the Auger process dramatically increases the heat yield at the high illumination power used for patterning. We found nanocrystals with higher photoluminescence quantum yields required a higher dosage to generate enough heat to complete the thermal transition on the surface, thus achieving a decent pattern contrast. For example, a good pattern of InP/ZnS (PLQY: 97%) required a dosage of 150 mJ cm^{-2}, while CdSe/ZnS (PLQY: 40−70%) required a dosage of 80−100 mJ cm^{-2} and CdSe (PLQY: 5−20%) required only 20−25 mJ cm^{-2}. For CdSe QDs with no shell, it is reasonable to assume that the majority of absorbed energy will be converted to heat. This heat can increase the local temperature, diffuse into lower temperature regions, or radiate to the atmosphere with an emissivity of about 0.6.[45]

When heat flows into a material, its temperature increases in proportion to the amount of heat divided by the amount of the material, described by $\rho C_P \partial T/\partial t + \rho C_P \boldsymbol{u} \nabla T$, where ρ is the material density, C_P is specific heat capacity, T is the absolute temperature, and $\boldsymbol{u}$ is the velocity vector for heat flux. Heat will

https://doi.org/10.1021/jacs.2c03672
J. Am. Chem. Soc. 2022, 144, 10495−10506

flow from hotter regions to adjacent colder regions, in proportion to the temperature gradient and the thermal conductivity k of the material, described by $-k\nabla T$. In summary, assuming the material has no thermoelastic damping, the heat diffusion follows the equation: $Q = \rho C_P \partial T/\partial t + \rho C_P \boldsymbol{u}\nabla T - k\nabla T$.

The heat supply q is the only energy source. It can be expressed as

$$q = \frac{2P}{\pi r_{\text{spot}}^2} e^{-(2r_{\text{focus}}^2/r_{\text{spot}}^2)} \times f(t) \times w \times \epsilon \quad (3)$$

where the first exponential term, with the pre-exponential factor, is related to the energy density distribution within the Gaussian beam, in which P is the laser power, r_{spot} is the laser spot size, r_{focus} is the distance from a certain point to the central point of the laser focal plane, and $f(t)$ describes the time-dependence of light intensity, such as pulse duration. w accounts for incomplete light-to-heat conversion efficiency due to film reflectivity. ϵ is the emissivity of CdSe film. In our model, the NC layer is exposed to a 10 ns light pulse, followed by rapid cooling and $f(t) = 1$ for $0 < t < 10$ nm and 0 otherwise.

Temperature Distribution Profile. The COMSOL Multiphysics package was used to model the heating and cooling profiles defined by the light exposure and thermal diffusion among the material and substrate layers (Figure 6C−E and Animation S1). During the 10 ns laser pulse, the temperature of the NC layer promptly increases due to local laser heating. The temperature in the beam center can reach as high as ∼1400 K at $t = 10$ ns, followed by rapid cooling when the energy supply is cut off until the sample reaches thermal equilibrium. Finally, the entire film starts cooling, with the rate determined by thermal radiation and boundary thermal diffusion.

The patterned region should not only reach a specific temperature threshold, e.g., the ligand decomposition onset temperature (T_{on}), but also be held at a high temperature for a time sufficient for enough ligands to decompose. With the first-order rate law assumption and the kinetic parameters experimentally derived for CME ligands, the reaction time required to pattern NCs ($C > 95\%$, as illustrated in Figure 1E) at different temperatures can be calculated (Table S3). For example, CdSe-CME film should remain above 1000 K for 11 ns, above 900 K for 104 ns, or above 800 K for 1.7 μs to completely dissociate the CME ligands. If the region fails to remain at this temperature for the minimum time required to fully dissociate the surface ligands, NCs may remain soluble, and no pattern can be formed during development.

The rapid cooling results from thermal emission into the ambient environment and vertical heat diffusion into the substrate layer, which typically has a larger thermal diffusivity than the patterned NC layer (Table S2), so that the substrate acts as a heat sink. Vertical thermal diffusion into the substrate is more favorable for substrates with high thermal conductivity, as demonstrated by the comparison of simulated HIPIN temperature profiles for silica glass and silicon as the substrates. When silicon with high thermal conductivity is used as a substrate, the layer of patterned CdSe NCs cools more rapidly, just as observed in a previous study (Figure S21).[19] The suppression of in-plane heat conductivity is favorable for thermal patterning with high lateral resolution. The use of a thinner layer of patterned NCs also decreases thermal diffusion length in the less thermally conductive NC layer and facilitates material cooling through vertical thermal diffusion into the substrate (Figures S17−S21).

HIPIN Contrast Defined by NC Solubility Change. Because of the nonlinear relationship between the temperature and ligand conversion fraction (C), temperature profiles cannot be solely used to describe the patterning contrast. To address this point, our approach convolved heat generation, diffusion, and temperature-dependent reaction kinetics. We integrated the temperature profile using the reaction activation energy E_a and pre-exponential factor Z to plot spatial distributions of C values based on the Arrhenius equation and first-order rate law assumption (see Section S4 in the Supporting Information):

$$C = 1 - \exp\left[\int_0^\infty Z \exp\left(-\frac{E_a}{RT(t)}\right) dt\right] \quad (4)$$

The combination of fast cooling with suppressed horizontal in-plane heat diffusion due to the low thermal conductivity of the patterned NC layer and the exponential acceleration of ligand conversion kinetics with temperature creates a very sharp threshold between the regions with $C \approx 1$ and $C = 0$, as indicated by a very narrow, sub-100 nm transition layer (Figures 6E, S22, and 23). The simulated pattern feature size is 1.16 μm (2 × radius), which is comparable to the experimentally observed value of 1.76 μm (Figure 6B,E). We view this agreement as reasonable, given the simplicity of our computational model, which did not account for possible multistep reaction kinetics, etc.

The effective parameters E_a and Z for the ligand conversion reaction play an important role in the HIPIN pattern resolution in addition to the thermal diffusivities discussed previously. When reducing E_a from 168 to 100 kJ mol^{-1}, the pattern feature size increases, and resolution worsens (Figures S24 and S25). This observation provides guidance for the design of future thermally patternable NC inks and resists. Based on our computational analysis and previous experimental and theoretical studies, it should be possible to overcome the diffraction limit by thermal rather than photochemical patterning of NC inks.

CONCLUSIONS

In summary, we developed a thermal lithography method, HIPIN, which can directly pattern semiconductor, dielectric, and metal nanocrystals. We studied thermally induced reactions at NC surfaces and incorporated their kinetics into a model of the HIPIN process, thus obtaining the relationship between laser beam parameters and temperature profile, which will be useful in optimizing HIPIN for patterning thick films with high resolution. HIPIN can achieve a 480 nm feature size, which is comparable to the diffraction resolution limit. Based on theoretical models and simulations, HIPIN resolution can be further improved beyond the Abbe limit and used to fabricate ultrahigh-resolution devices. It can also maintain >78% of original PLQY and achieve ∼1.2 μm pattern thickness in highly light-absorbing semiconductor materials, which is a promising development for manufacturing highly efficient light-emitting quantum dot displays.

ASSOCIATED CONTENT

Supporting Information

The Supporting Information is available free of charge at https://pubs.acs.org/doi/10.1021/jacs.2c03672.

https://doi.org/10.1021/jacs.2c03672
J. Am. Chem. Soc. 2022, 144, 10495−10506

Materials, methods, supporting tables and figures, beam profile test, and finite element simulation details (PDF)

Temperature profiles and light intensity distribution in CdSe-CME layer during simulation (Animation S1) (AVI)

AUTHOR INFORMATION

Corresponding Author

Dmitri V. Talapin − *Department of Chemistry and James Franck Institute, Chicago, Illinois 60637, United States; Pritzker School of Molecular Engineering, University of Chicago, Chicago, Illinois 60637, United States; Center for Nanoscale Materials, Argonne National Laboratory, Argonne, Illinois 60517, United States;* orcid.org/0000-0002-6414-8587; Email: dvtalapin@uchicago.edu

Authors

Haoqi Wu − *Department of Chemistry and James Franck Institute, Chicago, Illinois 60637, United States;* orcid.org/0000-0002-5722-5425

Yuanyuan Wang − *Department of Chemistry and James Franck Institute, Chicago, Illinois 60637, United States; School of Chemistry and Chemical Engineering, Nanjing University, Nanjing 210023, P. R. China;* orcid.org/0000-0003-3971-8362

Jaehyung Yu − *Department of Chemistry and James Franck Institute, Chicago, Illinois 60637, United States*

Jia-Ahn Pan − *Department of Chemistry and James Franck Institute, Chicago, Illinois 60637, United States;* orcid.org/0000-0001-6153-8611

Himchan Cho − *Department of Chemistry and James Franck Institute, Chicago, Illinois 60637, United States; Department of Materials Science and Engineering, KAIST, Daejeon 34141, Repulic of Korea*

Aritrajit Gupta − *Department of Chemistry and James Franck Institute, Chicago, Illinois 60637, United States;* orcid.org/0000-0001-9406-8986

Igor Coropceanu − *Department of Chemistry and James Franck Institute, Chicago, Illinois 60637, United States;* orcid.org/0000-0001-8057-1134

Chenkun Zhou − *Department of Chemistry and James Franck Institute, Chicago, Illinois 60637, United States;* orcid.org/0000-0001-9388-7517

Jiwoong Park − *Department of Chemistry and James Franck Institute, Chicago, Illinois 60637, United States; Pritzker School of Molecular Engineering, University of Chicago, Chicago, Illinois 60637, United States*

Complete contact information is available at: https://pubs.acs.org/10.1021/jacs.2c03672

Author Contributions

‖H.W. and Y.W. contributed equally to this work.

Notes

The authors declare no competing financial interest.

ACKNOWLEDGMENTS

The authors would like to thank A. Nelson for the thorough reading and editing of the manuscript. This work was supported by the National Science Foundation under Award Number CHE-1905290 and by the Department of Defense (DOD) Air Force Office of Scientific Research under Grant number FA9550-18-1-0099. D.V.T. acknowledges support from the Samsung Global Research Outreach Program on New Materials. This work was partially supported by the University of Chicago Materials Research Science and Engineering Center, which is funded by the National Science Foundation under Award Number DMR-2011854. Use of the Center for Nanoscale Materials, an Office of Science User Facilities operated for the U.S. Department of Energy (DOE) Office of Science by Argonne National Laboratory, was supported by the U.S. DOE under Contract No. DE-AC02-06CH11357. This work made use of the Pritzker Nanofabrication Facility, which receives partial support from the SHyNE Resource, a node of the National Science Foundation's National Nanotechnology Coordinated Infrastructure (NSF ECCS-2025633).

REFERENCES

(1) Bagher, A. M. Quantum Dot Display Technology and Comparison with OLED Display Technology. *Int. J. Adv. Res. Phys. Sci.* **2017**, *4*, 48−53.

(2) Tang, X.; Ackerman, M. M.; Chen, M.; Guyot-Sionnest, P. Dual-Band Infrared Imaging Using Stacked Colloidal Quantum Dot Photodiodes. *Nat. Photonics* **2019**, *13*, 277−282.

(3) Talapin, D. V.; Lee, J.-S.; Kovalenko, M. V.; Shevchenko, E. V. Prospects of Colloidal Nanocrystals for Electronic and Optoelectronic Applications. *Chem. Rev.* **2010**, *110*, 389−458.

(4) Choi, J. H.; Wang, H.; Oh, S. J.; Paik, T.; Sung, P.; Jo, P. S.; Sung, J.; Ye, X.; Zhao, T.; Diroll, B. T.; Murray, C. B. Exploiting the Colloidal Nanocrystal Library to Construct Electronic Devices. *Science* **2016**, *352*, 205−208.

(5) Kagan, C. R.; Lifshitz, E.; Sargent, E. H.; Talapin, D. V. Building Devices from Colloidal Quantum Dots. *Science* **2016**, *353*, No. aac5523.

(6) Gao, M.; Li, L.; Song, Y. Inkjet Printing Wearable Electronic Devices. *J. Mater. Chem. C* **2017**, *5*, 2971−2993.

(7) Kim, B. H.; Onses, M. S.; Lim, J. B.; Nam, S.; Oh, N.; Kim, H.; Yu, K. J.; Lee, J. W.; Kim, J. H.; Kang, S. K.; et al. High-Resolution Patterns of Quantum Dots Formed by Electrohydrodynamic Jet Printing for Light-Emitting Diodes. *Nano Lett.* **2015**, *15*, 969−973.

(8) Park, J. S.; Kyhm, J.; Kim, H. H.; Jeong, S.; Kang, J.; Lee, S. E.; Lee, K. T.; Park, K.; Barange, N.; Han, J.; et al. Alternative Patterning Process for Realization of Large-Area, Full-Color, Active Quantum Dot Display. *Nano Lett.* **2016**, *16*, 6946−6953.

(9) Yang, J.; Hahm, D.; Kim, K.; Rhee, S.; Lee, M.; Kim, S.; Chang, J. H.; Park, H. W.; Lim, J.; Lee, M.; et al. High-Resolution Patterning of Colloidal Quantum Dots via Non-Destructive, Light-Driven Ligand Crosslinking. *Nat. Commun.* **2020**, *11*, No. 2874.

(10) Lim, K. S.; Galarraga, J. H.; Cui, X.; Lindberg, G. C. J.; Burdick, J. A.; Woodfield, T. B. F. Fundamentals and Applications of Photo-Cross-Linking in Bioprinting. *Chem. Rev.* **2020**, *120*, 10662−10694.

(11) Wang, Y.; Fedin, I.; Zhang, H.; Talapin, D. V. Direct Optical Lithography of Functional Inorganic Nanomaterials. *Science* **2017**, *357*, 385−388.

(12) Wang, Y.; Pan, J. A.; Wu, H.; Talapin, D. V. Direct Wavelength-Selective Optical and Electron-Beam Lithography of Functional Inorganic Nanomaterials. *ACS Nano* **2019**, *13*, 13917−13931.

(13) Cho, H.; Pan, J. A.; Wu, H.; Lan, X.; Coropceanu, I.; Wang, Y.; Cho, W.; Hill, E. A.; Anderson, J. S.; Talapin, D. V. Direct Optical Patterning of Quantum Dot Light-Emitting Diodes via In Situ Ligand Exchange. *Adv. Mater.* **2020**, *32*, No. 2003805.

(14) Onyegam, E. U.; Mantey, J.; Rao, R. A.; Mathew, L.; Hilali, M.; Saha, S.; Jawarani, D.; Smith, S.; Ferrer, D. A.; Sreenivasan, S. V.; Banerjee, S. K. In *Exfoliated Sub-10 μm Thin Germanium for Cost-Effective Germanium Based Photovoltaic Applications*, 2011 37th IEEE Photovoltaic Specialists Conference, 2011; pp 000271−000273.

(15) Hasan, N. B.; Ghazi, R. A. Study Optical and Electrical Properties of Cd_{1-x} Zn_xS Thin Films Prepared by Spray Pyrolysis Technique. *Int. J. Eng. Adv. Res. Technol.* **2016**, *10*, 33−36.

(16) Kuznetsova, N. A.; Malkov, G. V.; Gribov, B. G. Photoacid Generators. Application and Current State of Development. *Russ. Chem. Rev.* **2020**, *89*, 173−190.
(17) Jiang, H.; Jin, S.; Wang, C.; Ma, R.; Song, Y.; Gao, M.; Liu, X.; Shen, A.; Cheng, G. J.; Deng, H. Nanoscale Laser Metallurgy and Patterning in Air Using MOFs. *J. Am. Chem. Soc.* **2019**, *141*, 5481−5489.
(18) Garcia, R.; Knoll, A. W.; Riedo, E. Advanced Scanning Probe Lithography. *Nat. Nanotechnol.* **2014**, *9*, 577−587.
(19) Wei, J.; Wang, Y.; Wu, Y. Manipulation of Heat-Diffusion Channel in Laser Thermal Lithography. *Opt. Express* **2014**, *22*, 32470−32480.
(20) Meng, Y.; Behera, J. K.; Wang, Z.; Zheng, J.; Wei, J.; Wu, L.; Wang, Y. Nanostructure Patterning of C-Sb_2Te_3 by Maskless Thermal Lithography Using Femtosecond Laser Pulses. *Appl. Surf. Sci.* **2020**, *508*, No. 145228.
(21) Howell, S. T.; Grushina, A.; Holzner, F.; Brugger, J. Thermal Scanning Probe Lithography—a Review. *Microsyst. Nanoeng.* **2020**, *6*, No. 21.
(22) Usami, Y.; Watanabe, T.; Kanazawa, Y.; Taga, K.; Kawai, H.; Ichikawa, K. 405 nm Laser Thermal Lithography of 40 nm Pattern Using Super Resolution Organic Resist Material. *Appl. Phys. Express* **2009**, *2*, No. 126502.
(23) Ong, W. L.; Rupich, S. M.; Talapin, D. V.; McGaughey, A. J. H.; Malen, J. A. Surface Chemistry Mediates Thermal Transport in Three-Dimensional Nanocrystal Arrays. *Nat. Mater.* **2013**, *12*, 410−415.
(24) Usami, Y.; Watanabe, T.; Kanazawa, Y.; Taga, K.; Kawai, H.; Ichikawa, K. 405 Nm Laser Thermal Lithography of 40 Nm Pattern Using Super Resolution Organic Resist Material. *Appl. Phys. Express* **2009**, *2*, No. 126502.
(25) Liu, X.; Sachan, A. K.; Howell, S. T.; Conde-Rubio, A.; Knoll, A. W.; Boero, G.; Zenobi, R.; Brugger, J. Thermomechanical Nanostraining of Two-Dimensional Materials. *Nano Lett.* **2020**, *20*, 8250−8257.
(26) Wang, D.; Kodali, V. K.; Underwood, W. D.; Jarvholm, J. E.; Okada, T.; Jones, S. C.; Rumi, M.; Dai, Z.; King, W. P.; Marder, S. R.; Curtis, J. E.; Riedo, E. Thermochemical Nanolithography of Multifunctional Nanotemplates for Assembling Nano-Objects. *Adv. Funct. Mater.* **2009**, *19*, 3696−3702.
(27) Lee, W. K.; Dai, Z.; King, W. P.; Sheehan, P. E. Maskless Nanoscale Writing of Nanoparticle-Polymer Composites and Nanoparticle Assemblies Using Thermal Nanoprobes. *Nano Lett.* **2010**, *10*, 129−133.
(28) Kim, W. J.; Vidal, X.; Baev, A.; Jee, H. S.; Swihart, M. T.; Prasad, P. N. Photothermal-Reaction-Assisted Two-Photon Lithography of Silver Nanocrystals Capped with Thermally Cleavable Ligands. *Appl. Phys. Lett.* **2011**, *98*, No. 133110.
(29) Huang, C. M.; Yeh, C. H.; Chen, L.; Huang, D. A.; Kuo, C. Energetic-Assisted Scanning Thermal Lithography for Patterning Silver Nanoparticles in Polymer Films. *ACS Appl. Mater. Interfaces* **2013**, *5*, 120−127.
(30) Ooms, M. D.; Jeyaram, Y.; Sinton, D. Disposable Plasmonics: Rapid and Inexpensive Large Area Patterning of Plasmonic Structures with CO_2 Laser Annealing. *Langmuir* **2015**, *31*, 5252−5258.
(31) Belman, N.; Israelachvili, J. N.; Li, Y.; Safinya, C. R.; Bernstein, J.; Golan, Y. The Temperature-Dependent Structure of Alkylamines and Their Corresponding Alkylammonium-Alkylcarbamates. *J. Am. Chem. Soc.* **2009**, *131*, 9107−9113.
(32) Knoll, A. W.; Pires, D.; Coulembier, O.; Dubois, P.; Hedrick, J. L.; Frommer, J.; Duerig, U. Probe-Based 3-D Nanolithography Using Self-Amplified Depolymerization Polymers. *Adv. Mater.* **2010**, *22*, 3361−3365.
(33) Wang, F.; Diesendruck, C. E. Polyphthalaldehyde: Synthesis, Derivatives, and Applications. *Macromol. Rapid Commun.* **2018**, *39*, No. 1700519.
(34) Dong, A.; Ye, X.; Chen, J.; Kang, Y.; Gordon, T.; Kikkawa, J. M.; Murray, C. B. A Generalized Ligand-Exchange Strategy Enabling Sequential Surface Functionalization of Colloidal Nanocrystals. *J. Am. Chem. Soc.* **2011**, *133*, 998−1006.
(35) Rosen, E. L.; Buonsanti, R.; Llordes, A.; Sawvel, A. M.; Milliron, D. J.; Helms, B. A. Exceptionally Mild Reactive Stripping of Native Ligands from Nanocrystal Surfaces by Using Meerwein's Salt. *Angew. Chem., Int. Ed.* **2012**, *51*, 684−689.
(36) Štorha, A.; Mun, E. A.; Khutoryanskiy, V. V. Synthesis of Thiolated and Acrylated Nanoparticles Using Thiol-Ene Click Chemistry: Towards Novel Mucoadhesive Materials for Drug Delivery. *RSC Adv.* **2013**, *3*, 12275−12279.
(37) Li, B.; Liu, W.; Yan, L.; Zhu, X.; Yang, Y.; Yang, Q. Revealing Mechanisms of PL Properties at High and Low Temperature Regimes in CdSe/ZnS Core/Shell Quantum Dots. *J. Appl. Phys.* **2018**, *124*, No. 044302.
(38) Chen, P. E.; Anderson, N. C.; Norman, Z. M.; Owen, J. S. Tight Binding of Carboxylate, Phosphonate, and Carbamate Anions to Stoichiometric CdSe Nanocrystals. *J. Am. Chem. Soc.* **2017**, *139*, 3227−3236.
(39) Liu, Z.; Lin, C. H.; Hyun, B. R.; Sher, C. W.; Lv, Z.; Luo, B.; Jiang, F.; Wu, T.; Ho, C. H.; Kuo, H. C.; He, J. Micro-Light-Emitting Diodes with Quantum Dots in Display Technology. *Light: Sci. Appl.* **2020**, *9*, No. 83.
(40) Flynn, J. H.; Wall, L. A. A Quick.Direct Method for the Determination of Activation Energy from Thermogravimetric Data. *J. Polym. Sci., Part B: Polym. Lett.* **1966**, *4*, 323−328.
(41) Sauerbrunn, S.; Gill, P. *Decomposition Kinetics Using TGA*; TA Instruments: New Castle, Delaware, 1994.
(42) Hamizi, N. A.; Johan, M. R. Optical Properties of CdSe Quantum Dots via Non-TOP Based Route. *Int. J. Electrochem. Sci.* **2012**, *7*, 8458−8467.
(43) Jasieniak, J.; Smith, L.; Van Embden, J.; Mulvaney, P.; Califano, M. Re-Examination of the Size-Dependent Absorption Properties of CdSe Quantum Dots. *J. Phys. Chem. C* **2009**, *113*, 19468−19474.
(44) Hanifi, D. A.; Bronstein, N. D.; Koscher, B. A.; Nett, Z.; Swabeck, J. K.; Takano, K.; Schwartzberg, A. M.; Maserati, L.; et al.*et al.* Redefining Near-Unity Luminescence in Quantum Dots with Photothermal Threshold Quantum Yield. *Science* **2019**, *363*, 1199−1202.
(45) Bu, X.; Zhou, Y.; Zhang, T.; He, M. Preparation of Optically Active Substituted Polyacetylene@CdSe Quantum Dots Composites and Their Application for Low Infrared Emissivity. *J. Mater. Sci.* **2014**, *49*, 7133−7142.

https://doi.org/10.1021/jacs.2c03672
J. Am. Chem. Soc. 2022, 144, 10495−10506